ACS MATERIALS LETTERS

www.acsmaterialsletters.org

Structure and Electrocatalytic Performance of Cocrystallized Ternary Molybdenum Oxosulfide Clusters for Efficient Water Splitting

Biswajit Mondal,[▽] Arijit Jana,[▽] Jayoti Roy,[▽] Astrid Campos Mata, Akhil S. Nair, Ananthu Mahendranath, Soumyabrata Roy, Biswarup Pathak,* Pulickel M. Ajayan,* and Thalappil Pradeep*

Cite This: *ACS Materials Lett.* 2023, 5, 3306−3315

Read Online

ACCESS | Metrics & More | Article Recommendations | Supporting Information

ABSTRACT: **Polyoxometalates (POMs) belong to a class of metal oxyanion clusters that hold enormous promise for a wide range of catalytic reactions, due to their structural diversity and the presence of redox-active metal centers and heteroatomic sites within the framework. In this study, we successfully determined the structures of the first cocrystallized ternary molybdenum oxo-sulfide clusters: $Mo_{12}NaO_{54}P_8C_{48}H_{40}$, $Mo_{12}NaS_2O_{52}P_8C_{48}H_{40}$, and $Mo_{12}NaS_6O_{48}P_8C_{48}H_{40}$, which are abbreviated as Mo_{12}, $Mo_{12}@S_2$, and $Mo_{12}@S_6$, respectively. Together, they are referred to as Mo_{12}-TC. These clusters exhibit nearly identical exterior structures, making them indistinguishable, leading to their cocrystallization in a single unit cell with 50%, 25%, and 25% occupancy for Mo_{12}, $Mo_{12}@S_2$, and $Mo_{12}@S_6$, respectively, and could not be separated easily. To confirm their molecular formulae and occupancy within a crystal, we conducted single-crystal X-ray diffraction (SCXRD) and high-resolution electrospray ionization−mass spectrometry (ESI-MS) studies. The clusters exhibit a dumbbell-like shape, with each terminal of the dumbbell comprising a hexagonal Mo_6 basal plane shielded by multiple oxo, and oxosulfide moieties for Mo_{12} and $Mo_{12}@S_2/Mo_{12}@S_6$ clusters, respectively. Additionally, the clusters are protected by a ligand shell consisting of vertically aligned phenylphosphonic acid (PPA). Mo_{12}-TC demonstrates promising activity for electrochemical hydrogen and oxygen evolution reactions (HER and OER). Mo_{12}-TC exhibits overpotentials of 0.262 and 0.413 V vs RHE to reach HER current densities (in H_2SO_4) of 10 and 100 mA cm^{-2}, respectively, and overpotentials of 0.45 and 0.787 V vs RHE to reach OER current densities (in KOH) of 10 and 100 mA cm^{-2}, respectively, stable up to 5000 cycles. Density functional theory (DFT) calculations further elucidate their electrocatalytic potential, revealing the presence of active sites within these molecular frameworks.**

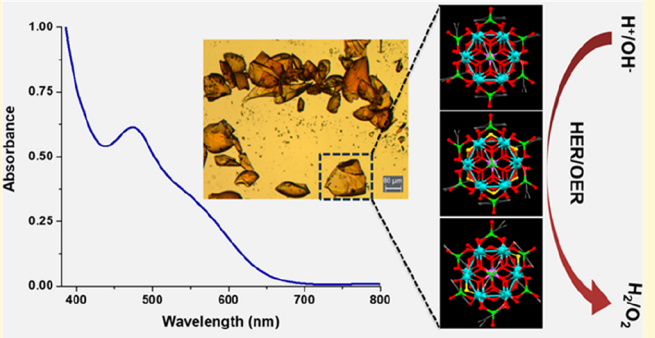

A diverse group of anionic polynuclear metal-oxo clusters (POMs), with a general formula $[M_mO_y]^{q-}$ (where M represents principally metals, such as Mo, W, V, and Nb), act as catalysts in a wide range of chemical transformations.[1−3] The continued interest in this field stems from the remarkable physical and chemical properties exhibited by these clusters, which arise from their flexible composition, structure, size, charge distribution, photochemistry, and redox chemistry.[4−9] The multidimensional assembly of these molecular cluster materials has led to the formation of various nanostructural and microstructural solids.[10,11] As conventional POM chemistry expands, it intersects with a range of scientific disciplines, including materials science, catalysis, nanotechnology, surface science, biology, magnetism, sensors, supramolecular materials, colloid science, memory devices, and molecular materials, thereby adding new dimensions to the field.[12−27]

Pristine POMs have certain drawbacks, such as low conductivity and tendency for aggregation, degradation, and leaching, which limit their applications. However, a funda-

Received: August 20, 2023
Revised: November 2, 2023
Accepted: November 8, 2023

Downloaded via INDIAN INST OF TECH MADRAS on November 19, 2023 at 14:55:52 (UTC).
See https://pubs.acs.org/sharingguidelines for options on how to legitimately share published articles.

© XXXX American Chemical Society

https://doi.org/10.1021/acsmaterialslett.3c00957
ACS Materials Lett. 2023, 5, 3306−3315

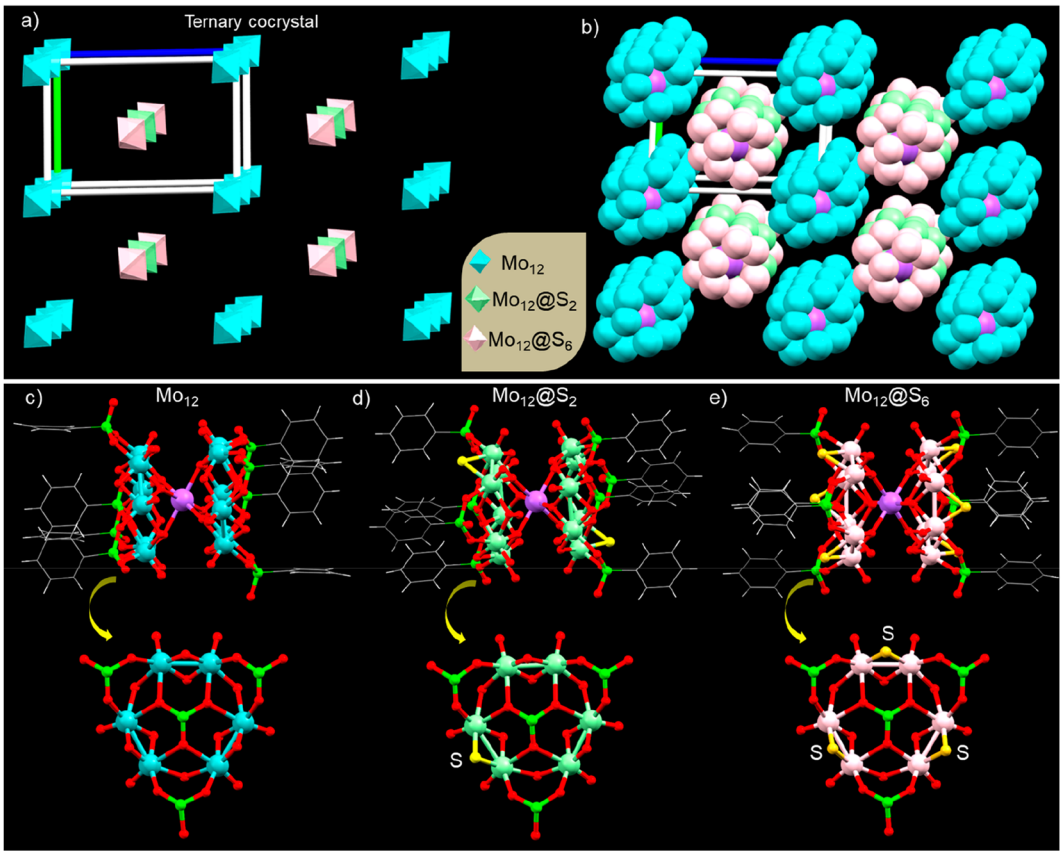

Figure 1. Single-crystal structures of the Mo_{12}-TC. (a) Schematic representation of the (2 × 2 × 2) unit cell of the ternary cocrystallized solid having the respective clusters. (b) Structural arrangement of the inner $NaMo_{12}$ units in the same lattice. The total molecular structures of (c) Mo_{12}, (d) $Mo_{12}@S_2$, and (e) $Mo_{12}@S_6$ clusters including PPA ligands. [Color labels: sky blue, pink, and light green = Mo; yellow = S; red = O, green = P, purple = Na; gray = C, white = H.]

mental characteristic of POMs is their ease of functionalization through the introduction of metal ions and other ligands.[28] This process of functionalization is widely employed to modify existing properties or introduce new ones, which is particularly valuable in catalysis, molecular magnetism, electrochemistry, dye-sensitized solar cells, and electrochemical water splitting.[2,3,28] Derivatization involves the incorporation of specific metallic centers into the polyoxometalate frameworks.[29,30] Alternatively, functionalization can be achieved by substituting oxo ligands with others, such as cyclopentadienyl derivatives, nitrogen-containing ligands, or sulfides. Introducing soft donating centers, such as S atoms, into the POM framework offers the potential for the emergence of novel properties. Since both O and S are constituents of group 6A within the periodic table, their chemical properties are very similar and substitution reactions between them are prone to occur.[31] S-coordinated transition-metal-based POMs are efficient catalysts, due to their ability to facilitate electron and proton transfer, which is crucial for electrocatalytic and photoelectrocatalytic processes like HER and OER.[32−40] Recently, capsules-like oxosulfur-based Mo-nanostructures encapsulated Ru nanoparticle was designed by Chen et al., which shows exceptional OER and HER dual activity and stability.[41] These systems exhibit excellent electrochemical properties characterized by a rapid and highly reversible redox activity. Amiinu et al. reported a cost-effective, operationally stable, multifunctional, and highly efficient vertically aligned MoS_2 electrocatalyst encapsulated with N-doped carbon frameworks.[42]

In the past five years, there have been discoveries of new types of cluster cocrystals. These solids consist of multiple clusters arranged in a lattice structure, resulting in new properties.[43,44] Several materials containing noble-metal clusters, particularly silver and copper clusters, have been structurally characterized during this period.[45−48] Indistinguishable arrangements of the surface ligands and ligand-specific interparticle interactions resulted in these solids. From the perspective of transition-metal clusters, Roy et al. have synthesized various binary cocrystallized solids by combining superatomic Co_6 and Cr_6 clusters with molecular C_{60} and C_{70} clusters.[49−51] These cocrystallized materials have demonstrated superconductive phonon and electron transport, polarized optical emission, and magnetic ordering behaviors, due to the electronic coupling of oppositely charged ionic species.[52−55] POMs also formed cocrystallized materials with proteins, peptides, polycyclic aromatic hydrocarbons, carbon nanotubes, and silver clusters, resulting in functional materials.[56−61]

By controlling the assembly of polyoxometallate clusters within a cocrystallized solid, it becomes possible to customize their properties, thus creating new opportunities to explore their potential applications. Despite this, the utilization of such cocrystallized solids in applications, particularly electrochemical water splitting, has been limited. In this work, we focused on the collective functional properties of cocrystallized molybdenum oxo-sulfide clusters. Through a conventional ambient wet chemical synthesis, we successfully synthesized mixed oxo-sulfide clusters of molybdenum. The resulting

https://doi.org/10.1021/acsmaterialslett.3c00957
ACS Materials Lett. 2023, 5, 3306−3315

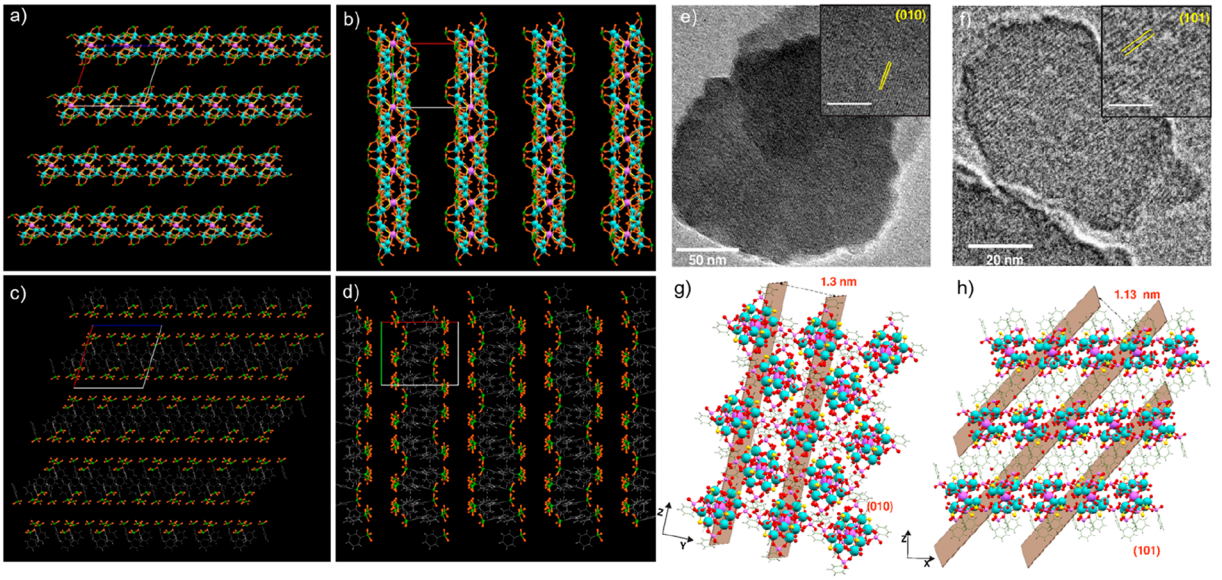

Figure 2. Supramolecular intercluster packing along the (a) *b* and (b) *c* crystallographic axes, and (c, d) corresponding packing of PPA ligands. (e, f) High-resolution TEM micrographs of the exfoliated layers of cocrystals. Inset show (010) and (101) lattice planes of the cocrystal, respectively. Intercluster packing along (g) (010) and (h) (101) lattice planes with marked interlayer spacings.

product consisted of three cocrystallized clusters (Mo_{12}, $Mo_{12}@S_2$, and $Mo_{12}@S_6$), as confirmed by single-crystal X-ray diffraction (SCXRD) and electron spray ionization−mass spectroscopy (ESI-MS) studies. Experimental and corroborative theoretical studies showed that these mixed clusters exhibit promising catalytic capabilities for electrochemical water splitting through active sites embedded within the molecular structures.

The following discussion pertains to the synthesis, structure, and characterization of cocrystallized clusters of Mo_{12}, $Mo_{12}@S_2$, and $Mo_{12}@S_6$. These clusters were prepared at room temperature through a one-step reduction process involving the precursors sodium molybdate ($NaMoO_4$) and sodium dithionite ($Na_2S_2O_4$). Upon introduction of a sulfur solution (obtained by dissolving solid sulfur in 50% ammonium sulfide solution) into aqueous $NaMoO_4$, the color of the reaction mixture changed from colorless to brown. Addition of $Na_2S_2O_4$ resulted in a darker shade of brown, indicating the formation of these clusters. The concentration of the solutions and various experimental parameters are presented in the Experimental Section in the Supporting Information. The clusters were purified through centrifugation (see the Experimental Section). A schematic of the detailed synthetic procedure is presented in the Experimental Section.

Single crystals were obtained after 30 days by the slow evaporation of the purified cluster in methanol at room temperature (25 °C). As-grown yellowish polyhedral crystals (shown in Figure S1 in the Supporting Information) were used for X-ray diffraction (XRD) and other experimental studies. Mo_{12}-TC crystallized in a monoclinic crystal system with the space group $P2_1/c$ (Table S1 in the Supporting Information). SCXRD study revealed that Mo_{12}-TC cocrystallized in a lattice, where eight Mo_{12} clusters were present in each corner of the unit cell, and the $Mo_{12}@S_2$ and $Mo_{12}@S_6$ clusters were present on the two opposite faces, having their occupancies of 50%, 25%, and 25%, respectively (shown in Figure S2 in the Supporting Information). Expanded views (2 × 2 × 2) of the lattice framework are shown in Figures 1a and 1b. Further analysis of these structures revealed that all three clusters have similar $NaMo_{12}$ kernels protected by oxo- and sulfido-moieties. For Mo_{12} clusters, 54 oxo- linkages were observed; however, for $Mo_{12}@S_2$ and $Mo_{12}@S_6$ clusters, two sulfido-52 oxo, and six sulphido-48 oxo linkages were observed, respectively (shown in Figures 1c, 1d, and 1e, as well as Figure S3 in the Supporting Information). The primary distinctions in the structures of these three clusters involve the replacement of two (found in $Mo_{12}@S_2$) and six dangling S linkages (found in $Mo_{12}@S_6$) with dangling O linkages. Four vertically aligned PPA ligands are shielded on each side of the metal-oxo-sulfide framework.

The core of these clusters, i.e., the $NaMo_{12}$ unit, consists of two hexagonal Mo_6 rings sandwiched with a Na atom connected through three oxo linkages (shown in Figure S4 in the Supporting Information). The distance between sodium and the centroid of the hexagonal Mo_6 unit is 2.35 Å (Figure S4). There are six short O···O interactions between these two dumbbell-shaped $Mo_6O_{27}P_4$ units having an average distance of ∼2.8 Å (shown in Figure S5a in the Supporting Information). These interactions are occurring between the μ_2 dangling oxygen of one unit with the μ_3 oxygen of the other unit. Such strong interactions are responsible for the structural rigidity of the two $Mo_6O_{27}P_4$ units. A similar type of ···O interaction was also observed for the other two clusters (see Figures S5b and S5c in the Supporting Information). Each Mo_6 unit of the cluster has three Mo_2 units, where the average Mo−Mo distance of the bonded Mo_2 unit is ∼2.62 Å, and the Mo−Mo distance between nonbonded units is 3.59 Å (Figure S6 in the Supporting Information). Each bonded Mo_2 unit is connected with sodium through an oxygen (Figure S3 in the Supporting Information) and each nonbonded Mo_2 unit is connected with one dangling O/S atom and one O atom, which is further connected to the central PPA unit (see Figures 1c−e). Each Mo is bonded with an isolated O having an average distance of 1.68 Å (Table S3 in the Supporting Information). The coordination mode of each Mo atom is

https://doi.org/10.1021/acsmaterialslett.3c00957
ACS Materials Lett. 2023, 5, 3306−3315

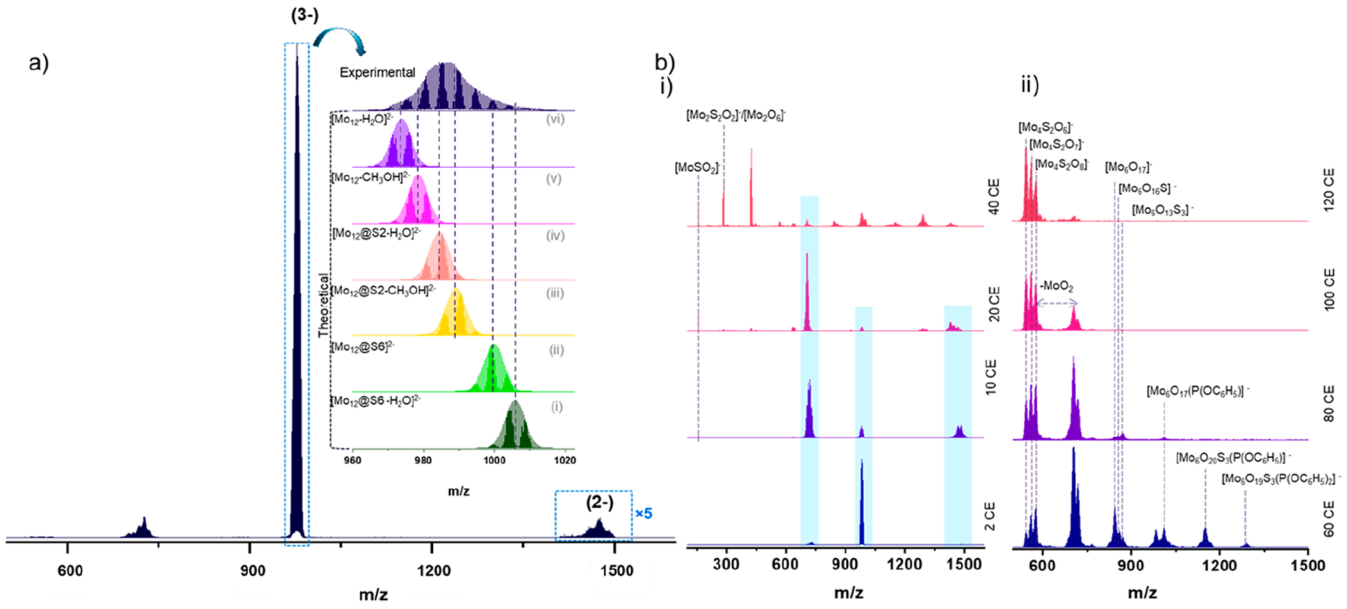

Figure 3. (a) High-resolution ESI-MS spectrum of the Mo_{12}-TC having an intense peak at m/z 989 and a mild peak at m/z 1484 in trianionic and dianionic charge states, respectively. Inset shows the exact matching of the experimental spectrum with the theoretical spectrum of the molecular compositions of cocrystallized clusters. (b) CE-dependent MS/MS fragmentation pattern of the major parent peak (m/z 989).

eight, and out of eight, seven are connected with O/S and one with a Mo atom (Figures 1c–e).

The binding of PPA ligands with the Mo atoms through Mo–O bonding is shown in Figure S7 in the Supporting Information. Each Mo_6 unit is connected with four PPA ligands, whereas the central PPA is connected with three oxygens arranged in a tripodal fashion and each oxygen is further bonded with a nonbonded Mo_2 unit in μ_2 mode. The other three PPA units are present at the periphery of the Mo_6 unit. Two O atoms of these three PPA ligands are connected with the Mo_6 unit, and the remaining one is free. The connected two O atoms are attached with Mo. Comparative P–O bond distances of different PPA ligands are presented in Table S4 in the Supporting Information. The average distance between central phosphorus and peripheral phosphorus is 4.68 Å, and the average distance between centroids of the central phenyl ring with the peripheral phenyl rings is ~4.84 Å (shown in Figure S7).

Supramolecular packing of these clusters along the different crystallographic axes is shown in Figures 2a and 2b, and the corresponding structures of ligands are also shown (Figures 2c and 2d). Careful analysis reveals that these clusters are packed in a layer-by-layer fashion along both the *a*- and *b*-axes. Careful analysis reveals that there are three types of intermolecular interactions (CH···π, CH···HC, and O···O; see Figure S8 in the Supporting Information). To visualize the layered intermolecular packing, we have directly imaged the single crystals using conventional transmission electron microscopy (TEM), following the technique developed in our group.[62] Although clusters are beam-sensitive, they could be imaged under appropriate conditions, as shown previously.[63] TEM micrographs of the ground cocrystals show different atomic layers with interlayer spacings of 1.30 and 1.13 nm (shown in Figures 2e and 2f) corresponding to lattice planes of (010) and (101), respectively, which are consistent with the interlayer spacing of Mo_{12} crystallites resolved from SCXRD (shown in Figures 2g and 2h).

The molecular composition of Mo_{12}-TC was analyzed using high-resolution ESI-MS investigations in the negative ion mode, after dissolving a few crystals in methanol (Figure 3a). In the mass spectrum, two broad peaks were detected within the m/z range of 950–1040 (as major peak) and m/z 1440–1640, representing trianionic and dianionic charge states, respectively. The trianionic peak observed at m/z 950–1040 corresponds to the molecular species of the three-clusters i.e., Mo_{12}, $Mo_{12}@S_2$, $Mo_{12}@S_6$ found in the crystal structure. Theoretical mass calculations revealed that the crystal consisted of these clusters and a certain number of water and methanol molecules that were derived from the solvent system. Similar solvent-associated peaks were also observed in other metal nanoclusters.[64−66] The broad isotopic distribution in the mass spectrum can be attributed to two factors: (1) molybdenum (Mo) has seven naturally stable isotopes, resulting in a wide isotopic distribution along with the contributions of naturally abundant isotopes from various atoms i.e., Na, O, S, C, P, and H present in the nanoclusters, and (2) the small mass differences ($\Delta m \approx 9–11$) between individual nanoclusters in their trianionic state. Additionally, these nanoclusters ionize by getting attached to one or two solvent molecules (H_2O = 18 and MeOH = 32), which further contributes to the broad distribution of a specific charge state observed.

In order to gain a deeper understanding of the structure, the peaks within the m/z range 950–1040 were subjected to collision-induced dissociation (CID) by isolating them within the ion trap. This isolation step aimed to eliminate other ionic species present in the gas phase. The selected ions were then subjected to sequential fragmentation upon collision with argon gas. Upon sequential increase of CE up to 20, the trianionic species underwent fragmentation through CID, resulting in two distinct sets of peaks at m/z 1436–1510 and m/z 690–740, with the charge state of −1 and −2, respectively (shown in Figure 3b). These peaks were attributed to the cleavage of the molybdenum nanoclusters, where

https://doi.org/10.1021/acsmaterialslett.3c00957
ACS Materials Lett. 2023, 5, 3306–3315

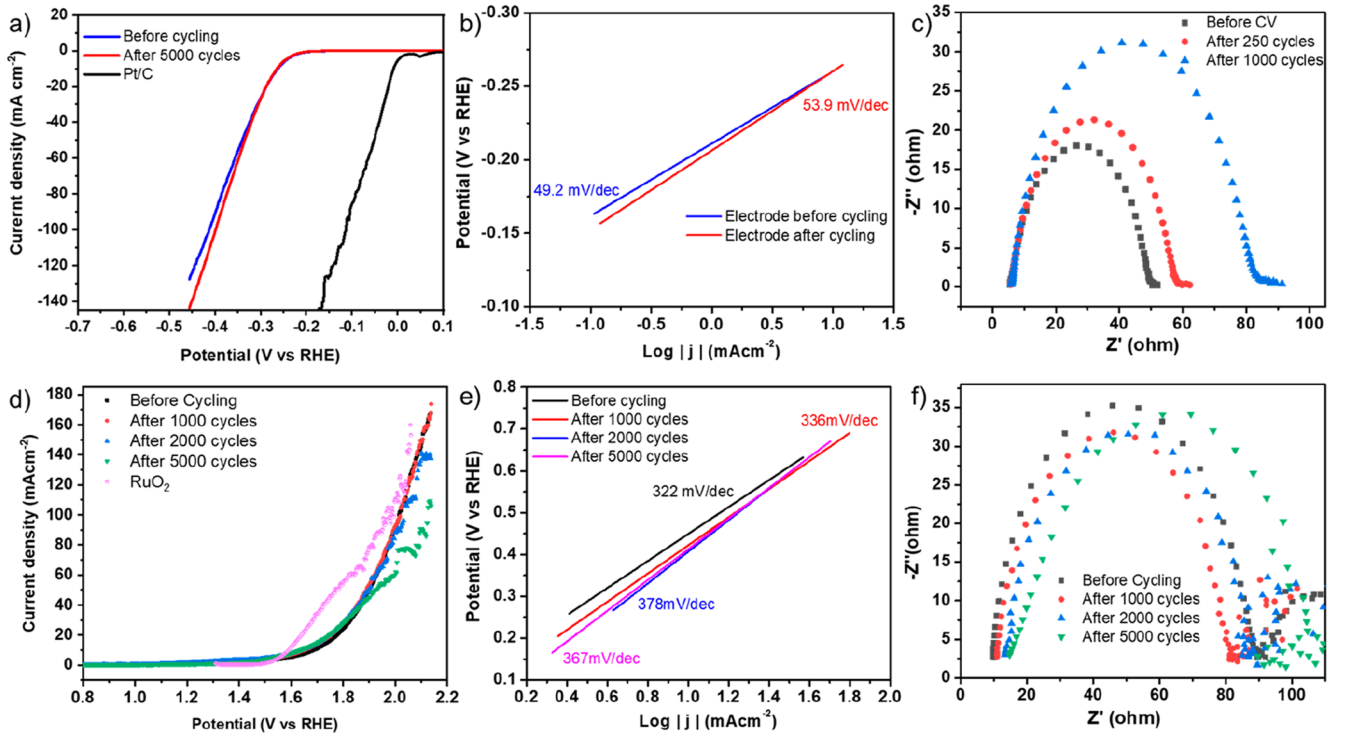

Figure 4. (a) Comparative LSV polarization curves of Mo_{12}-TC for HER before and after 5000 cycles. (b) Tafel plots of the polarization curves (before and after cycling). (c) EIS spectra showing R_{CT} during HER in 0.5 M H_2SO_4 at −0.256 V (vs RHE). (d) Comparative polarization curves of the Mo_{12}-TC catalyst clusters for the OER initially and after 1000, 2000, and 5000 cycles. (e) Tafel plots of the polarization curve (initially and after 1000, 2000, 5000 cycles) and (f) EIS spectra of cluster showing R_{CT} during the OER in 1.0 M KOH at 1.74 V (vs RHE).

fragments attached to Na were ionized as a monoanionic fragment, while the other half without Na was ionized as a dianionic fragment. As the applied collision energy reached the range of 10−20, H_2O and CH_3OH groups started to detach from the nanoclusters. The detachment confirmed the weak interaction between the solvent molecules and the parent nanoclusters.

At higher collisional energy (>20), two distinct pathways of fragmentation were observed. The first pathway involved the generation of fragment ions derived from sodiated fragment ions, while the second pathway involved fragments produced from the dianionic fragment ions. Both monoanionic and dianionic fragments simultaneously gave rise to constituent daughter ions as the collision energy was increased. Peripheral ligands attached to the nanoclusters, specifically PPA groups, were subsequently detached (occurring at an applied collisional energy of 60−80, as depicted in Figure 3b), followed by the fragmentation of the metal-oxo/sulfido kernels. This indicates direct binding of the PPA ligands at the peripheral sites of the nanoclusters. Fragmentation of the Mo−O−S core in the parent nanoclusters resulted in the formation of ions such as $[Mo_6O_{13}S_3]^-$, $[Mo_6O_{16}S]^-$, $[Mo_6O_{17}]^-$, $[Mo_4S_2O_8]^-$, $[Mo_4S_2O_7]^-$, and $[Mo_4S_2O_6]^-$ in the collision energy range of 100−120. Smaller fragment ions, including $[MoSO_2]^-$, $[Mo_2S_2O_2]^-$, and $[Mo_2O_6]^-$ ions, were detected at a lower m/z range. The sequential fragmentation observed during CID further supports the structural integrity of the clusters. The binding of PPA ligands was additionally confirmed by using FT-IR, which exhibited characteristic vibrational peaks at 1395 and 950 cm^{-1} corresponding to the P−O stretching and cage breathing modes, respectively (Figure S9 in the Supporting Information).

The catalytic HER performance of Mo_{12}-TC was evaluated in 0.5 M H_2SO_4 solution using a conventional three-electrode electrochemical setup. A graphite rod, a saturated calomel electrode (SCE), and the microcrystalline catalyst coated on glassy carbon (GC) electrode were used as the counter, reference, and working electrodes, respectively. Linear sweep voltammetry (LSV) polarization studies were performed to analyze the HER activity of the cluster at a scan rate of 5 mV s^{-1}, as presented in Figure 4a. The Mo_{12}-TC catalyst demonstrated promising HER activity that required an overpotential of 0.262 V to achieve a current density of 10 mA cm^{-2} and 0.413 V to reach a current density of 100 mA cm^{-2}. The stability of the cluster was assessed through an accelerated durability test between 0 and 0.4 V (vs RHE) at 100 mV s^{-1}. A small increase (2 mV) in overpotential (at 10 mAcm-2) was observed after 5000 cycles, indicating that these cocrystallized materials are stable for long-term use without a significant loss in catalytic performance (Figure 4a). The Tafel analysis (shown in Figure 4b), indicative of the electron transfer rate and mechanism (rate determining step) at the electrode−electrolyte interface, yielded a Tafel slope of 49.2 mV dec^{-1} for this catalyst. We infer that the obtained fast electron transfer at the interface resulted in enhanced HER activity through the Volmer−Heyrovsky mechanism.[67] The small increase (4.7 mV dec^{-1}) in the Tafel slope after cycling confirms the catalytic stability of Mo_{12}-TC. The charge-transfer resistance (R_{CT}) values for the cluster were calculated from electrochemical impedance spectroscopy (EIS), measured at a potential of −0.256 V vs RHE. The result is shown in Figure 4c

https://doi.org/10.1021/acsmaterialslett.3c00957
ACS Materials Lett. 2023, 5, 3306−3315

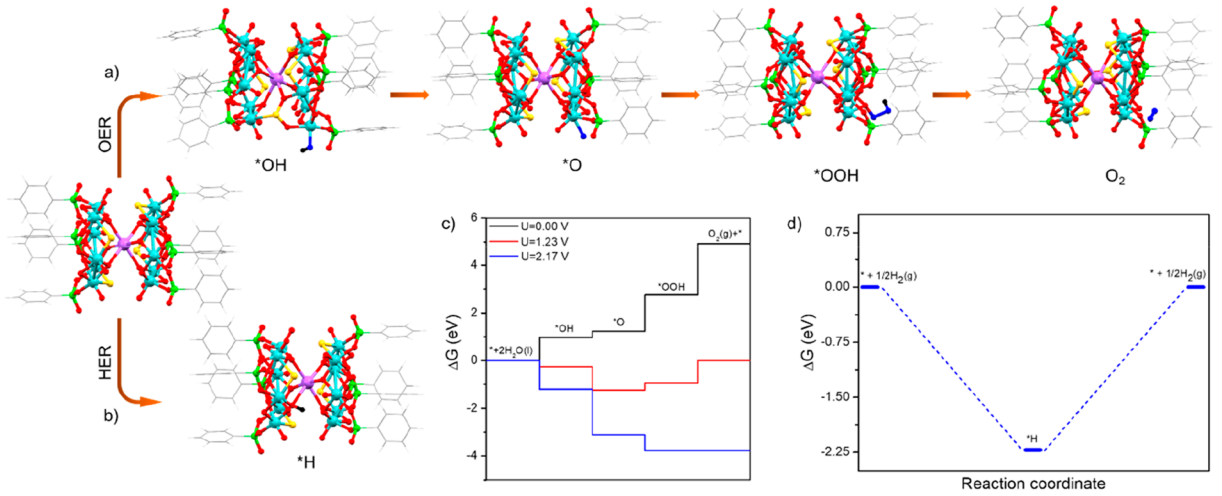

Figure 5. (a) Adsorption configurations of *OH, *O, and *OOH adduct intermediates and the O_2 end product of the $Mo_{12}@S_4$ cluster involved in the OER pathway. (b) Adsorption configuration of activated hydrogen species (*H) on the cluster. (c) Calculated OER free-energy profile for the cluster at different potentials. The free-energy profiles at 0 V (black), equilibrium potential of 1.23 V (red), and the limiting potential of 2.17 V (blue) are shown. (d) Free-energy profile of HER activity of the cluster. [Color labels: cyan = Mo; red = O, green = P, purple = Na, gray = C, white = H. The O and H atoms in the adsorption configurations of OER and HER intermediates are shown in blue and black, respectively.]

as a Nyquist plot, where the *x*- and *y*-axes are the real and negative imaginary parts of impedance, respectively. The Nyquist plots from the EIS spectra on the Mo_{12}-TC catalyst at different stages were fitted using equivalent Randles circuit models (as shown in Figures S10 and S11 in the Supporting Information) for accurately depicting the impedance behavior of the system and deconvoluting the components (series resistance, charge-transfer resistance, and constant phase elements) from the fitting parameters (as tabulated in Table S5 in the Supporting Information).

Figure 4c shows that R_{CT} does not change significantly after several cycles, with values of ∼44.1, ∼52.7, and ∼76.8 Ω for the cluster, in the beginning, after 250 cycles, and after 1000 cycles. The observed changes could be attributed to the formation of passivating layers on the electrode or the formation of bubbles during the measurement. These layers could hinder the transport of electrons and flow of reactants to and from the electrode surface, impeding the overall electrochemical process.

Although the LSV after 5000 cycles of the accelerated degradation test (ADT) shows slightly higher current in the more negative potential range, in the onset region, where the EIS was recorded, the 5000 C LSV is slightly left-shifted (compared to the pristine catalyst LSV) leading to higher R_{CT} values, as observed in the EIS studies. This effect was more pronounced during the initial cycling stages (first 500/1000 ADT cycles), until a more stable current and polarization curve was obtained after structural stabilization.

The electrocatalytic OER performance of Mo_{12}-TC was investigated in an alkaline medium (1 M KOH) using a similar cell setup. The polarization curves measured at a scan rate of 5 mV s^{-1} exhibit excellent activities for electrochemical OER with an onset potential (potential to reach a current density of 1 mA cm^{-2}) of ∼1.35 V (vs RHE) and overpotentials of 455, 545, 596, 635, and 787 mV at 10, 20, 30, 40, and 100 mA cm^{-2}, respectively (Figure 4d). The comparisons of the HER and OER catalytic performance of Mo_{12}-TC with the state-of-the-art Pt/C and RuO_2 catalysts are shown in Figures 4a and 4d, for reference. Figure 4d also depicts the LSVs after 1000, 2000, and 5000 cycles, showing no significant increase in overpotentials, indicating that these clusters are durable. The sudden shift (toward a more positive potential) in the OER LSV (beyond 1.9 V) after 5000 cycles is probably due to the accumulation and evolution of high amounts of bubbles on the nonporous electrode surface leading to poor electrode−electrolyte contact and materials falling off from the coated catalyst layer. Figure 4e shows the Tafel plots for the OER in the initial condition and after 1000, 2000, and 5000 cycles. The cluster exhibits a Tafel slope of 322 mV dec^{-1}, which increases slightly to 367 mV dec^{-1} after 5000 cycles. EIS study shows the R_{CT} value to be ∼78.7 Ω before cycling and ∼70.8, ∼72.8, ∼91.2 Ω after 1000, 2000, and 5000 cycles, respectively, at 1.74 V (vs RHE, ∼15 mA cm^{-2}) (Figure 4f). The increase in R_{CT} values after several cycles can be attributed to marginal deactivation of the catalyst during OER. Moreover, to understand the post-electrocatalytic stability, as well the stability of the catalyst in different electrolytes, various spectroscopic and diffraction studies, such as UV-vis, attenuated total reflectance Fourier transform infrared (FTIR), X-ray photoelectron spectroscopy (XPS), X-ray diffraction (XRD) and Raman studies of the Mo_{12}-TC were performed, as provided in Figures S12−S14 and Tables S6 and S7 in the Supporting Information. Based on these combined studies broadly, the catalyst was found to be structurally and chemically stable under the catalytic conditions. Observed fluctuations in the XPS studies can arise from various surface oxidized species, adsorbed chemicals, electrolytes, and impurities and some expected changes in the elemental oxidation states on the surface during electrocatalysis. Further, we performed cyclic voltammetry (CV) studies at different scan rates on Mo_{12}-TC coated electrodes in the acidic medium (Figure S15 in the Supporting Information) to determine the double layer capacitance (C_{dl}). The C_{dl} value, comparable to the ECSA (electrochemical active surface area) of the catalyst, was obtained from the current density in the anodic and

https://doi.org/10.1021/acsmaterialslett.3c00957
ACS Materials Lett. 2023, 5, 3306−3315

cathodic sweeps, ΔJ ($|j_{Cat} - j_{An}|$), vs scan rate plot as 0.5 mF cm^{-2}.[68]

Density functional theory (DFT) was employed to study the reaction mechanism of HER and OER over $Mo_{12}@S_4$ cluster using the Vienna Ab-Initio Simulation Package (VASP) with the Perdew–Burke–Ernzerhof (PBE) functional under generalized gradient approximation (GGA).[69−71] To circumvent the computational cost, we have modeled a single molecular unit of $Mo_{12}@S_4$ cluster and considered it for further calculations. DFT optimized structures of Mo_{12} and $Mo_{12}@S_4$ are shown in Figure S16 in the Supporting Information and the electron density maps of the frontier molecular orbitals of the cluster are shown in Figures S17 and S18 in the Supporting Information. We simulated the OER using a four-electron transfer reaction mechanism involving *O, *OH, and *OOH (where the asterisk symbol (*) denotes the adsorbed species) intermediates (Figure 5a). The most stable binding modes of these intermediates were found to be one-fold binding (Figure 5a). The intermediates *OH and *O exhibited binding to the Mo site, while the lowest-energy geometry for *OOH exhibited binding to the O site of the cluster. Figure 5c shows the free-energy change of each intermediate steps involved in the reaction, which is calculated via the following equation:

$$\Delta G = \Delta E + \Delta ZPE - T\Delta S \quad (1)$$

where T is the temperature (298 K) and E, ZPE, and S are the total energy, zero-point energy, and the entropy of adsorbed hydrogen, respectively. The computed Gibbs free energy changes for $H_2O \rightarrow$ *OH, *OH → *O, *O → *OOH and *OOH → $O_2(g)$ are 0.97, 0.26, 1.52, and 2.17 eV, respectively. The potential-determining step (PDS) of the reaction was found to be the transformation of *OOH into O_2 which could be attributed to the strong adsorption of *OOH at the O site, which reduces the feasibility of it undergoing further oxidation. The higher value for overpotential (0.94 eV) obtained from DFT calculations, with respect to the experiment, could be attributed to the single molecular unit approximation of the cluster as well as the absence of explicit solvent interactions and dynamic effects in the calculations, which may play a crucial role in determining the catalytic activity under experimental conditions. We have performed a comparative OER theoretical calculation using the Mo_{12} cluster (without any S atoms). The presence of S in the cluster not only facilitates the overall OER catalytic performance of the cluster but also reduces the overpotential of the reaction (see Figure S19 in the Supporting Information).

Similarly, we have studied the energetics of the HER event over the $Mo_{12}@S_4$. The free energy change (ΔG_{H^*}) of the formation of activated hydrogen species is −2.22 eV (Figure 5d). This supports the experimental observation that the cluster acts as an efficient HER catalyst. Figure 5b shows the adsorption configuration of active hydrogen (*H) on the cluster.

In summary, we presented a new type of cocrystallized structurally similar molybdenum oxo-sulfide clusters. These clusters were synthesized under ambient conditions by the reduction of $NaMoO_4$ and $Na_2S_2O_4$ precursors in the presence of S. Mo_{12}-TC was characterized using various characterization techniques (SCXRD, ESI-MS, FT-IR, etc.). SCXRD reveals that each unit cell consists of three clusters (Mo_{12}, $Mo_{12}@S_2$, and $Mo_{12}@S_6$) with 50%, 25%, and 25% occupancy, respectively. This POM has two oval-shaped Mo_6-oxo/sulfide units, which are connected with a Na atom through oxygen centers. High-resolution mass spectrometry showed the presence of these clusters in solution, and the CID-MS studies reveal the losses of MoOS, and MoO_2 fragments from the parent species, which further confirm the presence of oxygen and sulfur moieties in the structure. Furthermore, the intermolecular layers of these clusters present in the crystals were imaged directly using conventional transmission electron microscopy. The cocrystallized nanocluster catalyst performed excellently as inexpensive, efficient, and stable electrocatalysts for both HER and OER, requiring moderate overpotentials for reaching current densities of 100 mA cm^{-2}. The catalyst exhibits good electrocatalytic stability, retaining its activity and electron transfer kinetics after 5000 cycles. The mechanistic details of the clusters' water splitting activities were examined by DFT calculations, which identified the stable adsorption configurations: i.e., mixed oxo and sulfide sites for the OER, and Mo as energetically favorable sites for the HER activity.

■ ASSOCIATED CONTENT

Supporting Information

The Supporting Information is available free of charge at https://pubs.acs.org/doi/10.1021/acsmaterialslett.3c00957.

Details of chemical used, experimental section, instrumentation, X-ray crystallographic details, computational details, and additional experimental data (PDF)
Single-crystal X-ray data of nanocluster (CIF)
Single-crystal X-ray data of nanocluster (CIF)
Single-crystal X-ray data of nanocluster (CIF)
Single-crystal X-ray data of nanocluster (CIF)
Single-crystal X-ray data of nanocluster (CIF)
Single-crystal X-ray data of nanocluster (CIF)
Single-crystal X-ray data of nanocluster (CIF)
Single-crystal X-ray data of nanocluster (CIF)
Single-crystal X-ray data of nanocluster (CIF)
Single-crystal X-ray data of nanocluster (CIF)

■ AUTHOR INFORMATION

Corresponding Authors

Thalappil Pradeep − *DST Unit of Nanoscience (DST UNS) & Thematic Unit of Excellence (TUE), Department of Chemistry, Indian Institute of Technology–Madras, Chennai 600036, India; International Centre for Clean Water, Chennai 600113, India;* orcid.org/0000-0003-3174-534X; Email: pradeep@iitm.ac.in

Pulickel M. Ajayan − *Department of Materials Science and NanoEngineering, Rice University, Houston, Texas 77005, United States;* orcid.org/0000-0001-8323-7860; Email: ajayan@rice.edu

Biswarup Pathak − *Department of Chemistry, Indian Institute of Technology Indore, Indore 453552, India;* orcid.org/0000-0002-9972-9947; Email: biswarup@iiti.ac.in

Authors

Biswajit Mondal − *DST Unit of Nanoscience (DST UNS) & Thematic Unit of Excellence (TUE), Department of Chemistry, Indian Institute of Technology–Madras, Chennai 600036, India*

Arijit Jana − *DST Unit of Nanoscience (DST UNS) & Thematic Unit of Excellence (TUE), Department of Chemistry, Indian Institute of Technology–Madras, Chennai 600036, India*

https://doi.org/10.1021/acsmaterialslett.3c00957
ACS Materials Lett. 2023, 5, 3306−3315

Jayoti Roy − *DST Unit of Nanoscience (DST UNS) & Thematic Unit of Excellence (TUE), Department of Chemistry, Indian Institute of Technology−Madras, Chennai 600036, India*

Astrid Campos Mata − *Department of Materials Science and NanoEngineering, Rice University, Houston, Texas 77005, United States*

Akhil S. Nair − *Department of Chemistry, Indian Institute of Technology Indore, Indore 453552, India; The NOMAD Laboratory at the FHI of the Max-Planck Gesellschaft and IRIS-Adlershof of the Humboldt-Universität zu Berlin, Berlin 14195, , Germany;* orcid.org/0000-0001-5723-3970

Ananthu Mahendranath − *DST Unit of Nanoscience (DST UNS) & Thematic Unit of Excellence (TUE), Department of Chemistry, Indian Institute of Technology−Madras, Chennai 600036, India*

Soumyabrata Roy − *Department of Materials Science and NanoEngineering, Rice University, Houston, Texas 77005, United States*

Complete contact information is available at: https://pubs.acs.org/10.1021/acsmaterialslett.3c00957

Author Contributions

[▽]These authors contributed equally in this project. B.M. planned and designed the whole project, with input from T.P.; he synthesized the clusters and did the initial characterization. He wrote the first draft of the manuscript. A.J. helped in crystallization of clusters and also contributed to the production of figures and writing of the manuscript. J.R. helped in synthesis of clusters and carried out the MS study; she also contributed to the analysis of MS data. A.C.M. and S.R. conducted electrocatalytic measurements and characterizations of the cluster electrodes, contributed in the manuscript drafting and revisions under the supervision of P.M.A. A.S.N. performed theoretical calculations under the guidance of B.P. A.M. contributed to the analysis of TEM micrographs of crystals. T.P. supervised the whole project and finalized the manuscript.

Notes

The authors declare no competing financial interest.

■ ACKNOWLEDGMENTS

We thank the Sophisticated Analytical Instruments Facility, IIT Madras, and Sudhadevi Antharjanam for the SC-XRD measurements. We thank Babu Varghese for the refinement of SC-XRD data. B.M. thanks IIT Madras for the fellowship. T.P. acknowledges funding from the Centre of Excellence on Molecular Materials and Functions under the Institution of Eminence scheme of IIT Madras. We thank the Department of Science and Technology, Government of India, for continuous support of our research program.

■ REFERENCES

(1) Long, D. L.; Tsunashima, R.; Cronin, L. Polyoxometalates: Building Blocks for Functional Nanoscale Systems. *Angew. Chem. - Int. Ed.* **2010**, *49*, 1736−1758.

(2) Wang, S. S.; Yang, G. Y. Recent Advances in Polyoxometalate-Catalyzed Reactions. *Chem. Rev.* **2015**, *115* (11), 4893−4962.

(3) Azmani, K.; Besora, M.; Soriano-López, J.; Landolsi, M.; Teillout, A. L.; de Oliveira, P.; Mbomekallé, I. M.; Poblet, J. M.; Galán-Mascarós, J. R. Understanding Polyoxometalates as Water Oxidation Catalysts through Iron vs Cobalt Reactivity. *Chem. Sci.* **2021**, *12* (25), 8755−8766.

(4) Papaconstantinou, E.; Hiskia, A. Photochemistry and Photocatalysis by Polyoxometalates. In *Polyoxometalate Molecular Science*; Springer, Dordrecht, The Netherlands, 2003; pp 381−416, DOI: 10.1007/978-94-010-0091-8_13.

(5) Ye, J. C.; Chen, J. J.; Yuan, R. M.; Deng, D. R.; Zheng, M. S.; Cronin, L.; Dong, Q. F. Strategies to Explore and Develop Reversible Redox Reactions of Li-S in Electrode Architectures Using Silver-Polyoxometalate Clusters. *J. Am. Chem. Soc.* **2018**, *140* (8), 3134−3138.

(6) Lei, J.; Yang, J.-J.; Liu, T.; Yuan, R.-M.; Deng, D.-R.; Zheng, M.-S.; Chen, J.-J.; Cronin, L.; Dong, Q.-F. Tuning Redox Active Polyoxometalates for Efficient Electron-Coupled Proton-Buffer-Mediated Water Splitting. *Chem.−Eur. J.* **2019**, *25* (49), 11432−11436.

(7) Streb, C.; Kastner, K.; Tucher, J. Polyoxometalates in Photocatalysis. In *Chemical Photocatalysis*; Walter de Gruyter GmbH, 2020; pp 363−378, DOI: 10.1515/9783110576764-015.

(8) Streb, C. New Trends in Polyoxometalate Photoredox Chemistry: From Photosensitisation to Water Oxidation Catalysis. *Dalton Trans.* **2012**, *41* (6), 1651−1659.

(9) Gumerova, N. I.; Rompel, A. Synthesis, Structures and Applications of Electron-Rich Polyoxometalates. *Nat. Rev. Chem.* **2018**, *2* (2), 1−20.

(10) Yu, B.; Zhao, X.; Ni, J.; Yang, F. Multiscale Assembly of Polyoxometalates: From Clusters to Materials. *ChemPhysMater.* **2023**, *2* (1), 20−29.

(11) Piot, M.; Abécassis, B.; Brouri, D.; Troufflard, C.; Proust, A.; Izzet, G. Control of the Hierarchical Self-Assembly of Polyoxometalate-Based Metallomacrocycles by Redox Trigger and Solvent Composition. *Proc. Natl. Acad. Sci. U.S.A.* **2018**, *115* (36), 8895−8900.

(12) Ni, L.; Li, H.; Xu, H.; Shen, C.; Liu, R.; Xie, J.; Zhang, F.; Chen, C.; Zhao, H.; Zuo, T.; Diao, G. Self-Assembled Supramolecular Polyoxometalate Hybrid Architecture as a Multifunctional Oxidation Catalyst. *ACS Appl. Mater. Interfaces* **2019**, *11* (42), 38708−38718.

(13) Stuckart, M.; Monakhov, K. Y. Polyoxometalates as Components of Supramolecular Assemblies. *Chem. Sci.* **2019**, *10* (16), 4364−4376.

(14) Roy, S.; Crans, D. C.; Parac-Vogt, T. N. Editorial: Polyoxometalates in Catalysis, Biology, Energy and Materials Science. *Front. Chem.* **2019**, *7*, 646.

(15) Gumerova, N. I.; Rompel, A. Interweaving Disciplines to Advance Chemistry: Applying Polyoxometalates in Biology. *Inorg. Chem.* **2021**, *60* (9), 6109−6114.

(16) Busche, C.; Vilà-Nadal, L.; Yan, J.; Miras, H. N.; Long, D. L.; Georgiev, V. P.; Asenov, A.; Pedersen, R. H.; Gadegaard, N.; Mirza, M. M.; Paul, D. J.; Poblet, J. M.; Cronin, L. Design and Fabrication of Memory Devices Based on Nanoscale Polyoxometalate Clusters. *Nature* **2014**, *515* (7528), 545−549.

(17) Veríssimo, M. I. S.; Evtuguin, D. V.; Gomes, M. T. S. R. Polyoxometalate Functionalized Sensors: A Review. *Front. Chem.* **2022**, *10*, 840657.

(18) Chen, L.; Chen, W. L.; Wang, X. L.; Li, Y. G.; Su, Z. M.; Wang, E. B. Polyoxometalates in Dye-Sensitized Solar Cells. *Chem. Soc. Rev.* **2019**, *48* (1), 260−284.

(19) Shi, D.; Zheng, R.; Liu, C.-S.; Chen, D. M.; Zhao, J.; Du, M. Dual-Functionalized Mixed Keggin- and Lindqvist-Type Cu24-Based POM@MOF for Visible-Light-Driven H2 and O2 Evolution. *Inorg. Chem.* **2019**, *58* (11), 7229−7235.

(20) Paille, G.; Gomez-Mingot, M.; Roch-Marchal, C.; Haouas, M.; Benseghir, Y.; Pino, T.; Ha-Thi, M. H.; Landrot, G.; Mialane, P.; Fontecave, M.; Dolbecq, A.; Mellot-Draznieks, C. Thin Films of Fully Noble Metal-Free POM@MOF for Photocatalytic Water Oxidation. *ACS Appl. Mater. Interfaces* **2019**, *11* (51), 47837−47845.

(21) Qin, J. S.; Du, D. Y.; Guan, W.; Bo, X. J.; Li, Y. F.; Guo, L. P.; Su, Z. M.; Wang, Y. Y.; Lan, Y. Q.; Zhou, H. C. Ultrastable Polymolybdate-Based Metal-Organic Frameworks as Highly Active Electrocatalysts for Hydrogen Generation from Water. *J. Am. Chem. Soc.* **2015**, *137* (22), 7169−7177.

(22) Clemente-Juan, J. M.; Coronado, E.; Gaita-Ariño, A. Magnetic Polyoxometalates: From Molecular Magnetism to Molecular Spintronics and Quantum Computing. *Chem. Soc. Rev.* **2012**, *41* (22), 7464−7478.
(23) Zheng, S. T.; Yang, G. Y. Recent Advances in Paramagnetic-TM-Substituted Polyoxometalates (TM = Mn, Fe, Co, Ni, Cu). *Chem. Soc. Rev.* **2012**, *41* (22), 7623−7646.
(24) Duan, Y.; Clemente-Juan, J. M.; Giménez-Saiz, C.; Coronado, E. Large Magnetic Polyoxometalates Containing the Cobalt Cubane "$[Co^{III}Co_3^{II}(OH)_3(H_2O)_{6-m}(PW_9O_{34})]^{3-}$" ($m$ = 3 or 5) as a Subunit. *Front. Chem.* **2018**, *6*, 231.
(25) Luo, Z.; Kögerler, P.; Cao, R.; Hill, C. L. Synthesis, Structure, and Magnetism of a Polyoxometalate with Coordinatively Unsaturated d-Electron-Transition Metal Centers. *Inorg. Chem.* **2009**, *48* (16), 7812−7817.
(26) Čolović, M. B.; Lacković, M.; Lalatović, J.; Mougharbel, A. S.; Kortz, U.; Krstić, D. Z. Polyoxometalates in Biomedicine: Update and Overview. *Curr. Med. Chem.* **2020**, *27* (3), 362−379.
(27) Bijelic, A.; Aureliano, M.; Rompel, A. Polyoxometalates as Potential Next-Generation Metallodrugs in the Combat Against Cancer. *Angew. Chem., Int. Ed.* **2019**, *58* (10), 2980−2999.
(28) Dolbecq, A.; Dumas, E.; Mayer, C. R.; Mialane, P. Hybrid Organic-Inorganic Polyoxometalate Compounds: From Structural Diversity to Applications. *Chem. Rev.* **2010**, *110* (10), 6009−6048.
(29) Liu, R.; Cao, K.; Clark, A. H.; Lu, P.; Anjass, M.; Biskupek, J.; Kaiser, U.; Zhang, G.; Streb, C. Top-down Synthesis of Polyoxometalate-like Sub-Nanometer Molybdenum-Oxo Clusters as High-Performance Electrocatalysts. *Chem. Sci.* **2020**, *11* (4), 1043−1051.
(30) Weinstock, I. A.; Schreiber, R. E.; Neumann, R. Dioxygen in Polyoxometalate Mediated Reactions. *Chem. Rev.* **2018**, *118* (5), 2680−2717.
(31) Zhang, G.; Wang, X. Oxysulfid-Halbleiter Für Die Photokatalytische Wasserspaltung Mit Sichtbarem Licht. *Angew. Chem.* **2019**, *131* (44), 15726−15728.
(32) Fielden, J.; Sumliner, J. M.; Han, N.; Geletii, Y. V.; Xiang, X.; Musaev, D. G.; Lian, T.; Hill, C. L. Water Splitting with Polyoxometalate-Treated Photoanodes: Enhancing Performance through Sensitizer Design. *Chem. Sci.* **2015**, *6* (10), 5531−5543.
(33) Salazar Marcano, D. E.; Moussawi, M. A.; Anyushin, A. V.; Lentink, S.; Van Meervelt, L.; Ivanović-Burmazović, I.; Parac-Vogt, T. N. Versatile Post-Functionalisation Strategy for the Formation of Modular Organic−Inorganic Polyoxometalate Hybrids. *Chem. Sci.* **2022**, *13* (10), 2891−2899.
(34) Roy, S.; Bagchi, D.; Vemuri, V.; Ch. Sarma, S.; Ahuja, V.; Rajaji, V.; Narayana, C.; Peter, S. C. Deconvolution of Phase−Size−Strain Effects in Metal Carbide Nanocrystals for Enhanced Hydrogen Evolution. *Nanoscale* **2020**, *12* (28), 15414−15425.
(35) Roy, S.; Vemuri, V.; Maiti, S.; Manoj, K. S.; Subbarao, U.; Peter, C. Two Keggin-Based Isostructural POMOF Hybrids: Synthesis, Crystal Structure, and Catalytic Properties. *Inorg. Chem.* **2018**, *57* (19), 12078−12092.
(36) Roy, S.; Mumbaraddi, D.; Jain, A.; George, S. J.; Peter, S. C. Crystal Engineering in Supramolecular Polyoxometalate Hybrids through PH Controlled in Situ Ligand Hydrolysis. *Inorg. Chem.* **2018**, *57* (2), 590−601.
(37) Roy, S.; Sarkar, S.; Pan, J.; Waghmare, U. V.; Dhanya, R.; Narayana, C.; Peter, S. C. Crystal Structure and Band Gap Engineering in Polyoxometalate-Based Inorganic−Organic Hybrids. *Inorg. Chem.* **2016**, *55* (7), 3364−3377.
(38) Sarma, S. Ch.; Mishra, V.; Mary, K. A. A.; Roy, S.; Peter, S. C. Inverse Strain Effect in Atomic Scale"—Enhanced Hydrogen Evolution Activity and Durability in Cu-Substituted Palladseite. *ACS Energy Lett.* **2018**, *3* (12), 3008−3014.
(39) Khan, M. A.; Al-Attas, T.; Roy, S.; Rahman, M. M.; Ghaffour, N.; Thangadurai, V.; Larter, S.; Hu, J.; Ajayan, P. M.; Kibria, M. G. Seawater Electrolysis for Hydrogen Production: A Solution Looking for a Problem? *Energy Environ. Sci.* **2021**, *14* (9), 4831−4839.
(40) Kumbhakar, P.; Parui, A.; Dhakar, S.; Paliwal, M.; Behera, R.; Gautam, A. R. S.; Roy, S.; Ajayan, P. M.; Sharma, S.; Singh, A. K.; Tiwary, C. S. Spontaneous Hydrogen Production Using Gadolinium Telluride. *iScience* **2023**, *26*, No. 106510.
(41) Chen, D.; Yu, R.; Wu, D.; Zhao, H.; Wang, P.; Zhu, J.; Ji, P.; Pu, Z.; Chen, L.; Yu, J.; Mu, S. Anion-Modulated Molybdenum Oxide Enclosed Ruthenium Nano-Capsules with Almost the Same Water Splitting Capability in Acidic and Alkaline Media. *Nano Energy* **2022**, *100*, No. 107445.
(42) Amiinu, I. S.; Pu, Z.; Liu, X.; Owusu, K. A.; Monestel, H. G. R.; Boakye, F. O.; Zhang, H.; Mu, S. Multifunctional Mo−N/C@MoS_2 Electrocatalysts for HER, OER, ORR, and Zn−Air Batteries. *Adv. Funct. Mater.* **2017**, *27* (44), 1702300.
(43) Bodiuzzaman, M.; Dar, A.; Pradeep, T. Cocrystals of Atomically Precise Noble Metal Nanoclusters. *Small* **2021**, *17* (27), 2003981.
(44) Wu, Z.; Yao, Q.; Zang, S.; Xie, J. Directed Self-Assembly of Ultrasmall Metal Nanoclusters. *ACS Mater. Lett.* **2019**, *1* (2), 237−248.
(45) Chai, J.; Yang, S.; Lv, Y.; Chen, T.; Wang, S.; Yu, H.; Zhu, M. A Unique Pair: Ag40 and Ag46 Nanoclusters with the Same Surface but Different Cores for Structure-Property Correlation. *J. Am. Chem. Soc.* **2018**, *140* (46), 15582−15585.
(46) Dar, W. A.; Bodiuzzaman, M.; Ghosh, D.; Paramasivam, G.; Khatun, E.; Sugi, K. S.; Pradeep, T. Interparticle Reactions between Silver Nanoclusters Leading to Product Cocrystals by Selective Cocrystallization. *ACS Nano* **2019**, *13* (11), 13365−13373.
(47) Liu, J. Y.; Alkan, F.; Wang, Z.; Zhang, Z. Y.; Kurmoo, M.; Yan, Z.; Zhao, Q. Q.; Aikens, C. M.; Tung, C. H.; Sun, D. Different Silver Nanoparticles in One Crystal: $Ag_{210}(^{i}PrPhS)_{71}(Ph_3P)_5Cl$ and $Ag_{211}(^{i}PrPhS)_{71}(Ph_3P)_6Cl$. *Angew. Chem.* **2019**, *58* (1), 195−199.
(48) Huang, J. H.; Liu, L. Y.; Wang, Z. Y.; Zang, S. Q.; Mak, T. C. W. Modular Cocrystallization of Customized Carboranylthiolate-Protected Copper Nanoclusters via Host-Guest Interactions. *ACS Nano* **2022**, *16* (11), 18789−18794.
(49) Roy, X.; Lee, C. H.; Crowther, A. C.; Schenck, C. L.; Besara, T.; Lalancette, R. A.; Siegrist, T.; Stephens, P. W.; Brus, L. E.; Kim, P.; Steigerwald, M. L.; Nuckolls, C. Nanoscale Atoms in Solid-State Chemistry. *Science (New York, N.Y.)* **2013**, *341* (6142), 157−160.
(50) Yang, J.; Russell, J. C.; Tao, S.; Lessio, M.; Wang, F.; Hartnett, A. C.; Peurifoy, S. R.; Doud, E. A.; O'Brien, E. S.; Gadjieva, N.; Reichman, D. R.; Zhu, X.; Crowther, A. C.; Billinge, S. J. L.; Roy, X.; Steigerwald, M. L.; Nuckolls, C. Superatomic Solid Solutions. *Nat. Chem.* **2021**, *13* (6), 607−613.
(51) Pinkard, A.; Champsaur, A. M.; Roy, X. Molecular Clusters: Nanoscale Building Blocks for Solid-State Materials. *Acc. Chem. Res.* **2018**, *51* (4), 919−929.
(52) O'Brien, E. S.; Trinh, M. T.; Kann, R. L.; Chen, J.; Elbaz, G. A.; Masurkar, A.; Atallah, T. L.; Paley, M. V.; Patel, N.; Paley, D. W.; Kymissis, I.; Crowther, A. C.; Millis, A. J.; Reichman, D. R.; Zhu, X. Y.; Roy, X. Single-Crystal-to-Single-Crystal Intercalation of a Low-Bandgap Superatomic Crystal. *Nat. Chem.* **2017**, *9* (12), 1170−1174.
(53) Ong, W. L.; O'Brien, E. S.; Dougherty, P. S. M.; Paley, D. W.; Higgs, C. F.; McGaughey, A. J. H.; Malen, J. A.; Roy, X. Orientational Order Controls Crystalline and Amorphous Thermal Transport in Superatomic Crystals. *Nat. Mater.* **2017**, *16* (1), 83−88.
(54) Handa, T.; Shih, P.; Koay, C. S.; Nuckolls, C.; Roy, X.; Berkelbach, T. C.; Zhu, X. Anisotropically Fused Clusters Form a 2D Superatomic Sheet Exhibiting Polarized Light Emission. *J. Phys. Chem. C* **2023**, *127* (3), 1519−1526.
(55) Lee, C. H.; Liu, L.; Bejger, C.; Turkiewicz, A.; Goko, T.; Arguello, C. J.; Frandsen, B. A.; Cheung, S. C.; Medina, T.; Munsie, T. J. S.; et al. Ferromagnetic Ordering in Superatomic Solids. *J. Am. Chem. Soc.* **2014**, *136* (48), 16926−16931.
(56) Bijelic, A.; Rompel, A. The Use of Polyoxometalates in Protein Crystallography - An Attempt to Widen a Well-Known Bottleneck. *Coord. Chem. Rev.* **2015**, *299*, 22−38.
(57) Soria-Carrera, H.; Atrí An-Blasco, E.; Martín-Rapun, R.; Mitchell, S. G. Polyoxometalate−Peptide Hybrid Materials: From Structure−Property Relationships to Applications. *Chem. Sci.* **2022**, *14* (1), 10−28.

https://doi.org/10.1021/acsmaterialslett.3c00957
ACS Materials Lett. 2023, 5, 3306−3315

(58) Le Magueres, P.; Hubig, S. M.; Lindeman, S. V.; Veya, P.; Kochi, J. K. Novel Charge-Transfer Materials via Cocrystallization of Planar Aromatic Donors and Spherical Polyoxometalate Acceptors. *J. Am. Chem. Soc.* **2000**, *122* (41), 10073−10082.
(59) Bosch-Navarro, C.; Matt, B.; Izzet, G.; Romero-Nieto, C.; Dirian, K.; Raya, A.; Molina, S. I.; Proust, A.; Guldi, D. M.; Martí-Gastaldo, C.; Coronado, E. Charge Transfer Interactions in Self-Assembled Single Walled Carbon Nanotubes/Dawson−Wells Polyoxometalate Hybrids. *Chem. Sci.* **2014**, *5* (11), 4346−4354.
(60) Wang, Z.; Su, H. F.; Tung, C. H.; Sun, D.; Zheng, L. S. Deciphering Synergetic Core-Shell Transformation from $[Mo_6O_{22}@Ag_{44}]$ to $[Mo_8O_{28}@Ag_{50}]$. *Nat. Commun.* **2018**, *9* (1), 1−8.
(61) Yonesato, K.; Yanai, D.; Yamazoe, S.; Yokogawa, D.; Kikuchi, T.; Yamaguchi, K.; Suzuki, K. Surface-Exposed Silver Nanoclusters inside Molecular Metal Oxide Cavities. *Nat. Chem.* **2023**, *15* (7), 940−947.
(62) Mahendranath, A.; Mondal, B.; Sugi, K. S.; Pradeep, T. Direct Imaging of Lattice Planes in Atomically Precise Noble Metal Cluster Crystals Using a Conventional Transmission Electron Microscope. *Chem. Commun.* **2022**, *58* (12), 1906−1909.
(63) Mahendranath, A.; Mondal, B.; Sugi, K. S.; Pradeep, T. Direct Imaging of Lattice Planes in Atomically Precise Noble Metal Cluster Crystals Using a Conventional Transmission Electron Microscope. *Chem. Commun.* **2022**, *58* (12), 1906−1909.
(64) Jana, A.; Chakraborty, P.; Dar, W. A.; Chandra, S.; Khatun, E.; Kannan, M. P.; Ras, R. H. A.; Pradeep, T. Dual Emitting Ag35 Nanocluster Protected by 2-Pyrene Imine Thiol. *Chem. Commun.* **2020**, *56* (83), 12550−12553.
(65) Jash, M.; Jana, A.; Poonia, A. K.; Khatun, E.; Chakraborty, P.; Nagar, A.; Ahuja, T.; Adarsh, K. V.; Pradeep, T. Phosphine-Protected Atomically Precise Silver-Gold Alloy Nanoclusters and Their Luminescent Superstructures. *Chem. Mater.* **2023**, *35* (1), 313−326.
(66) Roy, J.; Chakraborty, P.; Paramasivam, G.; Natarajan, G.; Pradeep, T. Gas Phase Ion Chemistry of Titanium−Oxofullerene with Ligated Solvents. *Phys. Chem. Chem. Phys.* **2022**, *24* (4), 2332−2343.
(67) Lasia, A. Mechanism and Kinetics of the Hydrogen Evolution Reaction. *Int. J. Hydrogen Energy* **2019**, *44* (36), 19484−19518.
(68) Roy, S.; Bagchi, D.; Dheer, L.; Sarma, S. C.; Rajaji, V.; Narayana, C.; Waghmare, U. V.; Peter, S. C. Mechanistic Insights into the Promotional Effect of Ni Substitution in Non-Noble Metal Carbides for Highly Enhanced Water Splitting. *Appl. Catal. B: Environ.* **2021**, *298*, No. 120560.
(69) Kresse, G.; Hafner, J. *Ab Initio* Molecular-Dynamics Simulation of the Liquid-Metal−Amorphous-Semiconductor Transition in Germanium. *Phys. Rev. B* **1994**, *49* (20), 14251.
(70) Perdew, J. P.; Chevary, J. A.; Vosko, S. H.; Jackson, K. A.; Pederson, M. R.; Singh, D. J.; Fiolhais, C. Atoms, Molecules, Solids, and Surfaces: Applications of the Generalized Gradient Approximation for Exchange and Correlation. *Phys. Rev. B* **1992**, *46* (11), 6671.
(71) Kresse, G.; Joubert, D. From Ultrasoft Pseudopotentials to the Projector Augmented-Wave Method. *Phys. Rev. B* **1999**, *59* (3), 1758.

https://doi.org/10.1021/acsmaterialslett.3c00957
ACS Materials Lett. 2023, 5, 3306−3315